IOP Publishing Phys. Med. Biol. 65 (2020) 235034 https://doi.org/10.1088/1361-6560/abc22f

Physics in Medicine & Biology

IPEM Institute of Physics and Engineering in Medicine

OPEN ACCESS

RECEIVED
28 May 2020

REVISED
10 October 2020

ACCEPTED FOR PUBLICATION
16 October 2020

PUBLISHED
27 November 2020

PAPER

Iterative micro-tomography of biopsy samples from truncated projections with quantitative gray values

A-L Robisch, J Frohn and T Salditt

Institut für Röntgenphysik, Georg-August-Universität Göttingen, Friedrich-Hund-Platz 1, 37077 Göttingen, Germany

E-mail: anna-lena.robisch@uni-goettingen.de

Keywords: micro-computed tomography, region of interest tomography, iterative tomographic reconstruction

Abstract

Three-dimensional reconstruction from truncated two-dimensional projections cannot be solved analytically without prior knowledge of the sample or access to the non-truncated projections. To suppress reconstruction artifacts in region of interest (ROI) or local tomography, an iterative algorithm has been devised based on back-projection and re-projection, assuming an approximately cylindrical shape of the entire sample of general homogeneity, which is especially applicable for micro-tomography of biopsy samples from biological tissue. Tomographic reconstruction is iteratively refined by minimizing the mismatch between an empty ROI and the reconstruction from the difference between measured sinogram and forward projected ROI reconstruction. By numerical simulation and experimental demonstration, it is shown that the algorithm is not only able to reconstruct quantitative gray values, but also to reduce artifacts of peripheral glow, and may lead to increased image sharpness. The method is particularly suitable for examination of biopsy/autopsy-samples of soft tissue by micro/nano-computed tomography.

1. Introduction

Micro- and nano-computed tomography (micro/nano-CT) is a technique to yield three-dimensional (3D) reconstructions of millimeter-sized samples with micrometer or sub-micrometer voxel sizes, down to the range of 50–100 nm, if nano-focused synchrotron radiation is used. Due to the commonly large aspect ratio between the total size of the sample and the volume of a single resolution element (voxel), and the necessity to avoid the detrimental influence of cutting and slicing during sample preparation, many micro/nano-CT applications can be categorized as so-called region of interest (ROI) tomography. In this case, tomographic reconstruction has to be performed using truncated projections which means that the entire object of interest is not or not completely visible in each projection. In other words, the field of view of the detector is not large enough to cover the whole object under every angle. Figure 1(a) illustrates a typical setting of ROI-tomography: A detector with limited field of view is rotated around a sample (gray circle). The ROI (white circle) contributes to each projection from 0° to 180°, yet each projection collects signal from different regions of the full sample. In the sketched configuration, only the parts colored in green and the white ROI contribute to the measured projection. None of the projections would contain the full object in lateral dimension.

Local tomography has been subject to numerous studies over the past decades (Wang and Yu 2013). In the following, two types of field of view have to be distinguished: (i) the field of view of the detector (dFOV) and (ii) the field of view of the reconstruction (rFOV). Due to the nature of tomographic back-projection, the rFOV is cylindrical (3D) or circular (two-dimensional (2D)), whereas the dFOV is reduced by one dimension with respect to the rFOV and is either a line or the active area of a 2D detector. If the dFOV is considerably smaller than the extent of the sample, tomographic reconstruction leads to various truncation artifacts.

Müller and Arce gave a detailed description and explanation of truncation artifacts (Müller and Arce 1996): objects which are completely inside the rFOV and hence visible in each and every projection are reconstructed without artifacts. Objects which are partially inside and partially outside the rFOV lead to circular tails along the outline of the rFOV. Objects which are completely outside the rFOV lead to two separate circular tails. Objects which are wrapped around the rFOV but do not have a contribution inside the rFOV lead to circular tails covering the full outline of the rFOV. Finally, it was found that gray values in the periphery of the rFOV are considerably elevated when reconstructing from truncated projections (Ohnesorge *et al* 2000). This peripheral glow becomes increasingly asymmetric with increasing distance of the ROI from the center of the full sample (Kyrieleis *et al* 2011). Note, however, that even if without strong shape artifacts, objects in the center of the rFOV also suffer from flawed gray levels, i.e. ROI reconstruction is not quantitative concerning the voxel values.

In fact, it can be shown mathematically that exact reconstruction of a ROI from a set of projections where truncation occurs in each image—the so-called interior problem—is not possible (Natterer 2001, Clackdoyle and Defrise 2010). A way out of this dilemma is access to additional *a priori* knowledge about the sample: Kudo *et al* as well as Ye *et al* have demonstrated that the interior problem of CT indeed can be solved, provided that knowledge on a sub-region inside the ROI is available (Kudo *et al* 2008, Ye *et al* 2007). More recently, local tomography algorithms making use of *a priori* knowledge of a sub-region have been proposed for example by Paleo *et al* (2017), Paleo and Mirone (2017).

Yet, *a priori* knowledge on the object inside the ROI is not always available. Different techniques have been devised to deal with the interior problem and to remove artifacts in the reconstruction. A popular strategy is to extend truncated sinograms. To this end, different implementations have been proposed: for example, Wagner and Ogawa *et al* have extended the measured projections by estimated values based on the complete shape of the sample (Wagner 1979, Ogawa *et al* 1984). Ohnesorge *et al* have extended truncated projections by symmetrically mirroring a defined range of projection values at the boundary of the sinogram and subsequent cosine weighting (Ohnesorge *et al* 2000). Hsieh *et al* have extended truncated sinograms by estimating the truncated region being due to water cylinders whose locations and radii can be determined from the measured projections (Hsieh *et al* 2004). Kyrieleis *et al* showed that extension of the truncated sinogram by adding pixels replicating the mean outermost projection values, suppresses peripheral glow (Kyrieleis *et al* 2011). This can be understood from the observation that artifacts at the edges of the rFOV are pushed outwards toward the artificially added voxels whereas features inside the rFOV are sufficiently well reconstructed. However, while sizes and shapes of objects inside the rFOV are retrieved, reconstructed gray values still cannot provide quantitative information: In fact, gray values are affected mainly—but importantly not only (Wang and Yu 2013)—by a constant offset (Kyrieleis *et al* 2011). This is known to compromise diagnosis in medical CT, and analytical power in material or biological studies by micro/nano-CT.

To overcome these limitations at least partly, about 40 years ago, Nalcioglu *et al* used low resolution scans of the entire sample to subtract contributions of external regions from high resolution but truncated projections (Nalcioglu *et al* 1979). Roughly at the same time, to reduce dose outside a ROI and to achieve artifact free reconstructions inside the ROI, Wagner *et al* recorded projections covering the whole sample but with varying dose inside and outside the ROI (Wagner 1979), followed by Yu *et al* who combined truncated and normal-dose projections with a few full and low-dose projections (Yu *et al* 2006). Less concerned with dose being one of the prime issues in medical CT, but rather with measurement time and quantitative gray values for a ROI, da Silva *et al* have combined full size and finely sampled projections recorded at coarsely distributed angular positions with truncated and equally finely sampled projections at intermediate angular positions such that the total number of projections is equal to the number of projections required for non-local tomography (da Silva *et al* 2018).

Apart from single step algorithms, iterative methods were composed in order to tackle the interior tomography problem. The common idea of these techniques is to minimize the difference between a known and a reconstructed quantity, i.e. the difference between a computed forward-projection and the measured data, based on iterative back-projection and re-projection (Nassi *et al* 1982, Kim *et al* 1985, Ogawa *et al* 1984). A particular but different case arises, if iterative tomography is chosen for sake of reconstruction quality, but cannot be carried out in the full projections due to computational load. In this context, Ziegler *et al* proposed to use full projections in order to first compute a complete tomographic reconstruction. Subsequently, the ROI was zeroed out from the slice, a sinogram of the region exterior to the ROI was computed and subtracted from the measured data. These modified projections were truncated and iterative reconstruction was finally applied to the modified and truncated projections (Ziegler *et al* 2008).

Iterative ROI tomography techniques have also been developed to reconstruct from truncated projections—in this case without the knowledge of the entire projection. An example is the method of

Azencott *et al* who stabilized iterative ROI reconstruction by wavelet-based regularization (Azencott *et al* 2018) and used truncated projections without access to the full non-truncated radiographs.

Iterative algorithms including maximum-likelihood methods take photon statistics into account. Maximum-likelihood methods have been successfully adapted to ROI tomography (Ziegler *et al* 2008, Zhang and Zeng 2007), and are capable of providing good reconstructions even when analytic methods fail (Zhang and Zeng 2007).

The need for quantitative gray value recovery in micro/nano-CT studies arises from the aim to extract material characteristics—such as electron density—from tomographic scans and establish a high resolution three dimensional map of the examined tissues containing specification of the different materials, i.e. as calcium-rich component or iron-rich component, thereby opening up new options and diagnostics for virtual histology.

The motivation of this work is to design a reconstruction method for micro-CT applications, where projections display only a small portion of the full sample (typically, inside a full slice of the sample the ROI covers about two percent) and where we require the reconstructed gray values to be quantitative in the sense that they agree with those that would be reconstructed from complete projections.

We further require that sample preparation can be designed to some degree: In particular, we are motivated by the case of biological tissue extracted by biopsies or autopsies for micro/nano-CT examination (see Töpperwien *et al* (2018), Robisch *et al* (2020)). In this case, samples taken out from a tissue block by using a biopsy punch are not of a diameter small enough to avoid ROI tomography, if high (nano-scale) resolution is required.

Hence, the desired tomographic reconstruction method needs to cope with fully truncated projections and needs to provide voxel-wise quantitative gray values. Importantly and in contrast to Ziegler *et al* (2008), no measurements of the full object are available.

In fact, in micro/nano-CT applications, the ROIs often amount to only a very small portion of the entire sample. For this reason, and keeping in mind that high resolution cameras (about 2048×2048 resolution elements) are used to record the truncated projections, it is challenging to simply extend the sinogram to the required amount of pixels. This is at least the case for methods where the sinogram has to be extended to match the size which full projections would have, so that the shape of the entire sample can be properly modeled. Note that this may not be required for all (analytical) shape corrections, but such methods are certainly far from being standard.

Because there is no single step unique solution to the interior problem, an iterative technique based on back-projection and re-projection was chosen.

Biopsy samples of biological tissue come with two general properties which we require for the proposed method: By the nature of sample preparation the shape of the entire sample is always cylindrical and the (soft) tissue is approximately homogeneous in density, i.e. its composition shows similar variations in structure sizes and similar variations from a mean index of refraction inside and outside the ROI. Furthermore, experiments are designed such that the axis of rotation always passes through the center of the ROI and that the relative position of the ROI with respect to the center of the full sample is known. The last requirement is always fulfilled when using motorized stages to align the axis of rotation centered in the dFOV as well as to position the sample with respect to the axis of rotation. With such configurations in mind, in this work, the central idea of the proposed method is to exploit the linearity of the Radon transform (Radon 1917) and to split the truncated sinogram in a contribution due to the material inside the ROI and a contribution from the material outside the ROI. The reconstructed ROI is refined in an iterative procedure which involves a geometry correction based on the path lengths through the full sample, repetitive steps of filtered back-projection (FBP) and subsequent forward-projection.

The manuscript is organized as follows: The introduction covering challenges and developments in local tomography is followed by section 2 which comprises the proposed ROI-reconstruction technique with a detailed description of the algorithm as well as illustration of its performance by simulations. Section 3 presents an application of the method to experimental data collected at a custom-built in-house micro-CT instrument. Finally, section 4 summarizes the key points of this work and puts it into a broader perspective.

2. Method and simulation

The general method for correcting artifacts resulting from tomographic reconstruction from truncated projections is to extend the sinogram artificially by replicating its outermost or mean outermost pixels as proposed in Kyrieleis *et al* (2011). However, as discussed in the introduction, the inverse Radon transform of an artificially extended sinogram does not allow the extraction of quantitative gray values. To make matters worse, due to memory and computational limitations, it can be challenging to extend the sinograms to the sizes of the non-truncated projections of the entire sample.

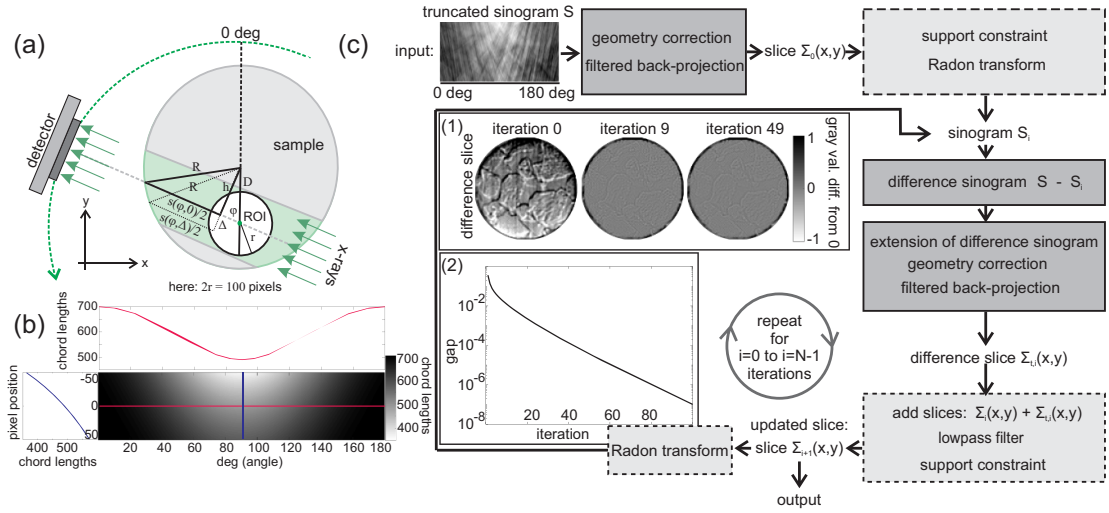

Figure 1. (a) Local tomography: Whereas ideally, one would like to record line integrals exclusively through the ROI (white circle), additional absorption of radiation inside the green regions cannot be avoided. (b) Position and angle dependent chord lengths of the full sample $s(\varphi, \Delta)$ for the geometry shown in (a) as well as two orthogonal profiles for constant angle and constant position, respectively. (c) Iterative scheme for tomography from truncated projections. Color code: light gray/dashed lines: (x, y)-space (slice); dark gray/solid lines: (φ, Δ)-space (sinogram). Inset (1): Difference slice used to update the reconstruction (see simulation in figure 2). Inset (2): Difference between successive iterates (see simulation in figure 2).

A way out is to include knowledge about the shape of the full sample as in Wagner (1979), Ziegler *et al* (2008). In the present work, we assume the sample to be of cylindrical shape and of almost isotropic content with similar variations inside and outside the ROI. This configuration is motivated by our goal in reconstructing native unstained tissue samples from biopsies and autopsies by micro/nano-CT. These tissues are characterized by small variation of the index of refraction around an average value (e.g. due to cellular nuclei, blood vessels, fibrous proteins etc). During the scan, the samples are kept inside a cylindrical polymer tube. With these restrictions, it becomes possible to analytically find correction values for each entry of the truncated sinogram. This allows reconstructing the approximately correct mean index of refraction inside the ROI.

Figure 1(a) illustrates a 2D section of a cylindrical sample with a highlighted ROI. By the nature of the Radon transform, the ROI itself is also circular/cylindrical. The axis of rotation is placed in the center of the ROI. Before reaching the detector, x-rays not only pass through the ROI itself (white circle in figure 1(a)), but also through its surrounding material (regions colored in light green in figure 1(a)). Hence, the accumulated absorption/phase shift encoded in the truncated sinogram is much larger than the accumulated absorption/phase shift corresponding to the ROI itself. The contribution of the surrounding material of the ROI can be estimated by the difference of the angle dependent chord lengths s through the full sample and those through the ROI s_r multiplied by an average gray value b per voxel.

Let the radius of the full sample be R. Given a ROI of radius $r < R$, the path lengths s_r through the circular ROI are found by

$$s_r(\Delta) = 2\left(r^2 - \Delta^2\right)^{1/2}, \tag{1}$$

where $\Delta \in]-r, r[$ is the shortest distance of $s_r(\Delta)$ to the center of the ROI. The calculation of the path lengths $s(\varphi, \Delta)$ through the entire sample requires some more information: the distance of the ROI with respect to the center of the sample $D = \sqrt{\delta_x^2 + \delta_y^2}$ (horizontal shift δ_x and vertical shift δ_y), as well as the radius R of the full sample, the angular position of the detector φ and the distance Δ inside the ROI with respect to its center. With the help of figure 1(a) and the Pythagorean theorem, one finds all possible chords $s(\varphi, \Delta)$ passing through sample and ROI under the angle φ and with distance Δ to the center of the ROI (see figures 1(a)–(b)):

$$s(\varphi, \Delta) = 2\left\{R^2 - [\Delta - aD\sin(\varphi + a\alpha)]^2\right\}^{1/2}, \tag{2}$$

$$\text{where} \begin{cases} \alpha = \arcsin(\delta_x/D)\ \&\ a = -1 & \text{for } \delta_y > 0 \\ \alpha = \arcsin(\delta_x/D)\ \&\ a = 1 & \text{for } \delta_y \le 0 \\ \alpha = 0\ \&\ a = -1 & \text{for } D = 0\,. \end{cases} \tag{3}$$

The variable a—being a sign—and the angular offset α are chosen such that they match the convention of `Matlab` regarding the coordinate system and the implementation of the Radon transform. The measured, truncated sinogram $\mathcal{S}(\varphi, \Delta)$ together with the path lengths $s(\varphi, \Delta)$ can be used to estimate the mean absorption b per voxel:

$$b = \frac{1}{MN} \sum_{m=1}^{M} \sum_{n=1}^{N} \frac{\mathcal{S}(\varphi_m, \Delta_n)}{s(\varphi_m, \Delta_n)} \,, \tag{4}$$

where M is the number of projections and N is the number of pixels. In order to compensate for the absorption outside the ROI, one can now subtract an offset $o(\varphi, \Delta)$ from the truncated sinogram:

$$o(\varphi, \Delta) := [s(\varphi, \Delta) - s_{\mathrm{r}}(\Delta)]\, b \,. \tag{5}$$

The gray values inside the ROI are reconstructed from $\mathcal{S}(\varphi, \Delta) - o(\varphi, \Delta)$. This geometric correction is necessary, but not sufficient. In fact, contrast and sharpness of the reconstructed structures and details inside the ROI turn out to be unsatisfactory, even if the gray value level has been corrected in this way. To increase sharpness and contrast, an iterative ansatz based on back-projection and re-projection is proposed as a second step. The underlying idea is to refine the tomographic reconstruction by using the truncated, measured sinogram $\mathcal{S}(\varphi, \Delta)$ and the Radon transform $\mathcal{S}_{i-1}(\varphi, \Delta)$ of the current estimate of the ROI, i.e. the solution from the previous iteration $i-1$, in the following way: The tomographic reconstruction (i.e. FBP) of $\mathcal{S}(\varphi, \Delta) - \mathcal{S}_{i-1}(\varphi, \Delta)$ is computed. If $\mathcal{S}_{i-1}(\varphi, \Delta)$ represents the Radon transform of the ROI already, one can expect gray values close to zero after tomographic reconstruction of the difference between the measured sinogram and the sinogram of the current iterate. Otherwise, one can expect that tomographic reconstruction of the difference sinogram still bears features inside the ROI that have not yet been reconstructed. These features are delivered by FBP of $\mathcal{S}(\varphi, \Delta) - \mathcal{S}_{i-1}(\varphi, \Delta)$ and are used to update the tomographic reconstruction of the current iterate in an additive way.

Figure 1(c) presents a schematic of the algorithmic workflow. Consider the initial iteration $i = 0$. The input of the algorithm is the measured, truncated sinogram $\mathcal{S}(\varphi, \Delta)$. The detector pixel size, the diameter of the full sample, and the relative position of the ROI with respect to the center of the full sample enter as known parameters, required to compute the angle dependent correction matrix $o(\varphi, \Delta)$ given in equation (5). The idea of the geometric correction is to reduce the projected gray values of the truncated sinogram according to the position and size of the ROI inside the sample by subtraction of an angle and pixel dependent offset. This offset approximates the contributions from regions outside the ROI. Thus, here, we modify the classical FBP operator $\mathcal{R}_f^{-1}$ (see e.g. Kak and Slaney (2001)) by including geometry as offset-subtraction:

$$\mathcal{R}_f^{-1}[\cdot] \to \mathcal{R}_{\mathrm{f,\,o}}^{-1}[\cdot] := \mathcal{R}_f^{-1}\left[\cdot - o(\varphi, \Delta)\right] \,. \tag{6}$$

A two dimensional slice $\Sigma_0(x, y) = \mathcal{R}_{\mathrm{f,\,o}}^{-1}\left[\mathcal{S}(\varphi, \Delta)\right]$ is calculated. For the current demonstration, FBP is implemented using the function `iradon` provided by `Matlab` with a Ram-Lak filter kernel and linear interpolation. Note that forward and backward projection can be replaced by any pair of functions or even iterative procedures that can handle tomographic projection and reconstruction. The reconstructed slice $\Sigma_0(x, y)$ is limited to the ROI (radius r) by application of a smooth support constraint:

$$\mathcal{P}_{\mathrm{s}}\left[\Sigma_0(x, y)\right] = \Sigma_0(x, y) \cdot \left[H(x, y) * G(x, y, \sigma = 1)\right] , \tag{7}$$

where $G(x, y, \sigma = 1)$ is a Gaussian filter kernel with standard deviation σ set to 1 pixel, $*$ symbolizes convolution and $H(x, y)$ is a circular hat profile

$$H(x, y) = \begin{cases} 1 & \text{for } \left(x^2 + y^2\right)^{1/2} \leq r \\ 0 & \text{else.} \end{cases} \tag{8}$$

The support-limited slice is used to compute a sinogram $\mathcal{S}_0(\varphi, \Delta)$ by the Radon transform $\mathcal{R}$:

$$\mathcal{S}_0(\varphi,\Delta) := \mathcal{R}\left[\mathcal{P}_s\left[\Sigma_0(x,y)\right]\right] . \tag{9}$$

The sinogram $\mathcal{S}_0(\varphi,\Delta)$ is subtracted from the measured sinogram $\mathcal{S}(\varphi,\Delta)$ resulting in a 'difference sinogram'. To reduce artifacts, the outermost pixels of the difference sinogram in the spatial direction are replicated. Next, a temporary or difference slice $\Sigma_{t,0}(x,y)$ is calculated:

$$\Sigma_{t,0}(x,y) = \mathcal{R}_{f,o}^{-1}\left[\mathcal{S}(\varphi,\Delta) - \mathcal{S}_0(\varphi,\Delta)\right] . \tag{10}$$

The motivation for the last step derives from the fact that subtraction of the re-projected sinogram $\mathcal{S}_0(\varphi,\Delta)$ from the measured sinogram $\mathcal{S}(\varphi,\Delta)$, must lead to a truncated sinogram of a sample with an empty ROI—provided that $\Sigma_0(x,y)$ has been a sufficiently accurate reconstruction of the ROI. The reason is found in the nature of the Radon transform itself, which is based on line integrals through the sample, or in the discrete case, on the summation of values along straight paths. However, as long as the difference slice displays features inside the ROI, the current reconstruction is not yet satisfactory. Inset (1) of figure 1(c) shows the difference slices $\Sigma_{t,0}(x,y)$, $\Sigma_{t,9}(x,y)$ and $\Sigma_{t,49}(x,y)$. In iteration 0, definitively, the difference slice $\Sigma_{t,0}(x,y)$ is not an empty ROI. The following step is to refine the reconstruction $\Sigma_0(x,y)$ by replacing the reconstructed slice $\Sigma_0(x,y)$ with the sum of $\Sigma_0(x,y)$ and $\Sigma_{t,0}(x,y)$:

$$\Sigma_1(x,y) = \Sigma_0(x,y) + \Sigma_{t,0}(x,y) . \tag{11}$$

As a consequence, missing features or low contrast in $\Sigma_0(x,y)$ but contained in $\Sigma_{t,0}(x,y)$ are recovered. To remove high frequency artifacts resulting from multiple forward and backward projections, a low-pass filter $L[\cdot]$ consisting of a two dimensional Gaussian filter kernel is applied. For the presented reconstructions, the standard deviation of the Gaussian filter kernel is set to 0.37 pixels in case of the noise free simulations, 0.47 pixels in case of the simulation containing noise and 0.35 pixels in case of the measured projections. Finally the reconstructed slice is confined to the ROI by the support constraint. In summary, one iteration i of the algorithm can be formulated as follows:

$$\Sigma_i(x,y) = \mathcal{P}_s L\left\{\Sigma_{i-1}(x,y) + \mathcal{R}_{f,o}^{-1}\left[\mathcal{S}(\varphi,\Delta) - \mathcal{S}_{i-1}(\varphi,\Delta)\right]\right\} , \tag{12}$$

where the initial iterate is

$$\Sigma_0(x,y) = \mathcal{P}_s\left\{\mathcal{R}_{f,o}^{-1}\left[\mathcal{S}(\varphi,\Delta)\right]\right\} \tag{13}$$

and where

$$\mathcal{S}_{i-1}(\varphi,\Delta) = \mathcal{R}\left[\Sigma_{i-1}(x,y)\right] . \tag{14}$$

The process is iterated until the difference slice $\mathcal{R}_{f,o}^{-1}\left[\mathcal{S}(\varphi,\Delta) - \mathcal{S}_{i-1}(\varphi,\Delta)\right]$ does not contain features different from noise anymore (see inlet (1) of figure 1(c)). Finally, convergence can be monitored by computing the gap $g(i)$ of successive iterates (see inlet (2) of figure 1(c)):

$$g(i) = \frac{1}{M}\sum_{x,y\in\mathrm{ROI}} \left|\Sigma_i(x,y) - \Sigma_{i-1}(x,y)\right| , \tag{15}$$

where here, M is the number of elements inside the ROI.

The described iterative procedure is tested by numerical simulations, with geometry as depicted in figure 2(a): a truncated sinogram of a circular sample consisting of $N/2 = 350$ pixels along radius R and embedded in an empty quadratic array of 1500 pixels side length, off-centered by 250 pixels in the y-direction is used. The embedding of the phantom in an empty background is necessary in order to simulate non-truncated projections with the axis of rotation passing through an off-centered sample. The sinogram is simulated using `Matlab`'s function `radon` applied to the embedded phantom.

The number of projections N_φ covering an angular range $\Delta\varphi$ of π is set to $N_\varphi = N\pi/2 \approx 1100$, fulfilling the angular sampling criterion for tomography and resulting in an angular step size of 0.16 deg. Note that for the angular sampling criterion, the spatial extent (here $N = 700$ pixels) of the sample rather than the full extent (here 1500 pixels) of sample and background has to be considered. The full noise-free sinogram (figure 2((d), top)) is truncated to a circular ROI of 100 pixels in diameter (figure 2((d), middle)). The corresponding ROI is marked by a light green circle and separately displayed in the bottom part of figure 2(a).

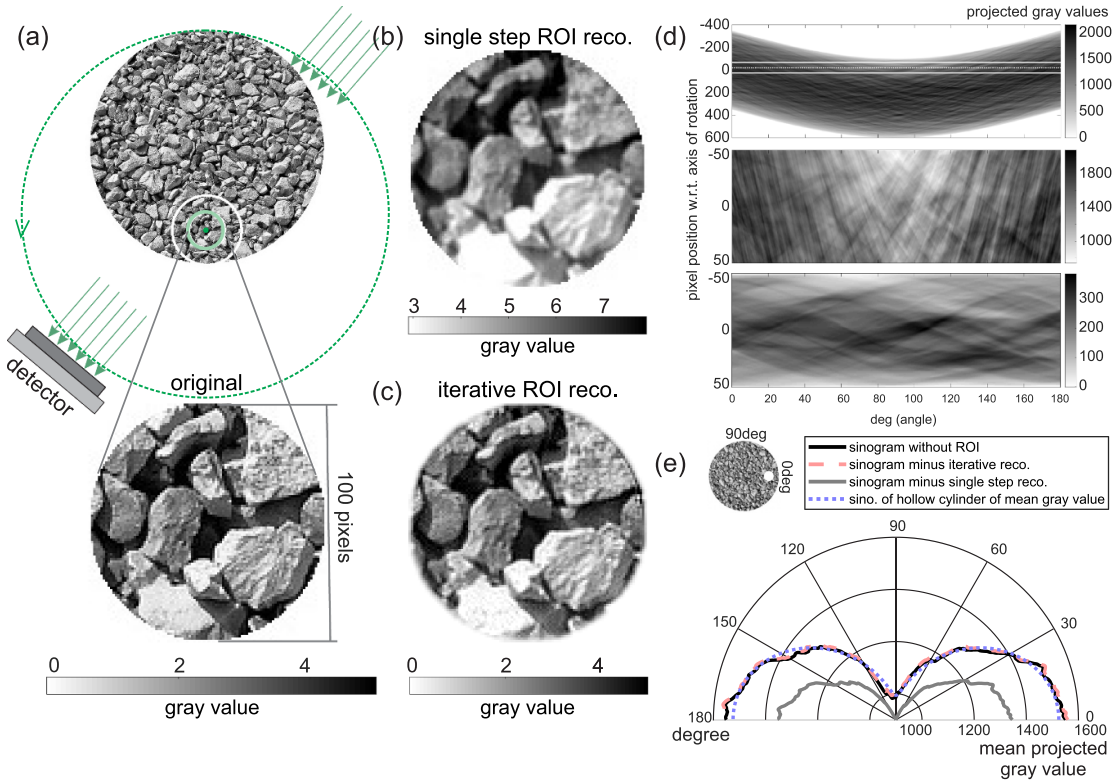

Figure 2. (a) Phantom for ROI-tomography. Truncated projections are simulated for a ROI consisting of 100 pixels in diameter and marked by a light green circle. The white circle enclosing the ROI represents the rFOV after artificially extending the truncated sinogram. The position of the axis of rotation is marked by a green dot and the dashed circle represents the positions of the detector. (b) Filtered back-projection of the extended truncated sinogram. (c) Iterative reconstruction of the truncated sinogram with quantitative recovery of gray values. (d) Sinogram of the full sample (top) with marked truncation region, truncated sinogram (middle) used for the reconstructions ((b)–(c)), sinogram of the iteratively reconstructed ROI (bottom). (e) Angle dependent, mean projected gray values outside the ROI computed by subtraction of the sinogram corresponding to the reconstructed ROI (see (d, bottom)) from the measured truncated sinogram (see (d, middle)).

First, the truncated sinogram (figure 2((d), middle)) is extended to twice its size by replicating the outermost gray values in positive and negative spatial direction. Its FBP is depicted in figure 2(b). Even though the reconstruction does not show typical truncation artifacts, it does not provide the correct gray values: Compared to the phantom shown in figure 2(a), the gray value level is considerably elevated. Without access to the ground truth, it is not possible to determine whether the reconstructed gray values coincide with those of the phantom.

Second, the truncated sinogram (figure 2((d), middle)) is reconstructed by the proposed iterative method. Based on the observation that successive iterates do not change significantly anymore, the algorithm is terminated after 100 iterations. The reconstructed ROI shown in figure 2(c) is very close to the true solution. In addition, figure 2((d), bottom) shows the sinogram simulated from the reconstruction of the ROI (figure 2(c)).

Figure 2(e) demonstrates that the iterative model including the geometry correction is a reasonable strategy to properly reconstruct gray values: The mean projected gray values outside the ROI estimated by equation (5) (dotted line) coincide well with the expected mean gray values extracted from the phantom without the ROI (black line). Structures and gray values inside the ROI were successfully reconstructed by the iterative procedure: The iteratively reconstructed ROI is subtracted from the phantom and the mean gray value outside the ROI (dashed curve in light red) coincides with that of the phantom (black curve). The same analysis is carried out for the reconstruction of the ROI by extending the sinogram. As expected, here the mean gray values deviate considerably (gray curve). Further, the image sharpness of the iterative reconstruction (c) is found to be enhanced compared to the reconstruction resulting from sinogram extension (b).

The benefit in resolution or sharpness and gray level accuracy is corroborated by comparison of the profiles shown in figures 3(a)–(c).

First, the cropped FBP reconstruction of the complete sinogram (figure 2((d), top)) of the phantom (figure 2((a), top)) is computed and compared to the original: The gray line in figure 3(a) shows the vertical profile through the central part of the ROI inside the phantom. The black line shows the profile through the

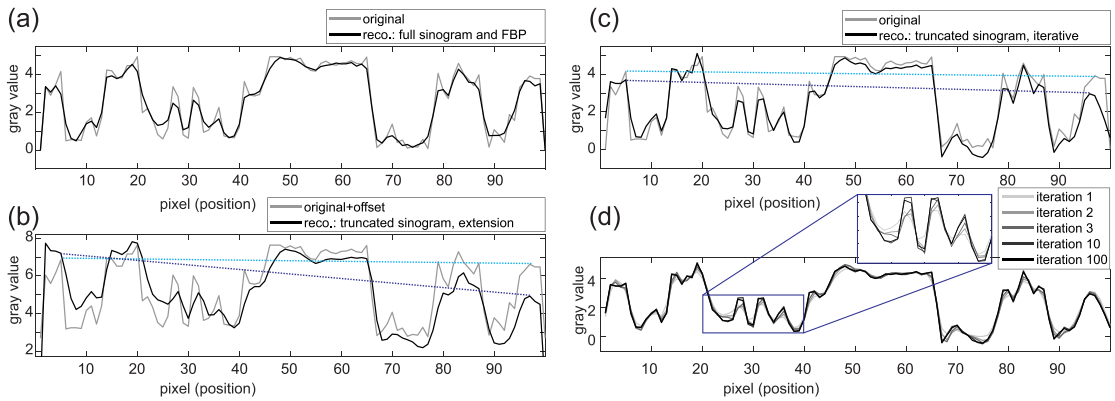

Figure 3. (a) Line profiles through phantom (figure 2((a), bottom), and gray line) and filtered back-projection of full sinogram (figure 2((d), top), and black line). (b) Line profiles through phantom (figure 2((a), bottom), and gray line) with shifted mean gray value and reconstruction from truncated sinogram by extension (figure 2(b), and black line). (c) Line profiles through phantom (figure 2((a), bottom), and gray line) and sinogram by iterative ROI-tomography (figure 2(c), and black line). (d) Line profiles through current estimate of the ROI in iterations 1, 2, 3, 10 and 100.

same pixels of the reconstruction by FBP. On the one hand, one clearly observes, that mean and relative gray values are preserved. This is expected since the reconstruction was computed from the full sinogram. On the other hand, the sharpness of the reconstruction is visibly decreased and high spatial frequencies are not fully retrieved. FBP or the specific `Matlab` implementation of FBP by the `iradon`-function with options `Ram-Lak` as filter and `linear` as interpolation method, seems to reduce the sharpness of the reconstruction with respect to the phantom. Second, the same vertical profile through the reconstruction of the truncated projections via sinogram-extension is shown against the true solution (figure 3(b)). Note that here, the mean value of the original gray values is shifted such that reconstruction and original can be easily compared. In addition to the decreased feature sharpness, which cannot exclusively be a consequence of local tomography (see figure 3(a)), an artificial gradient spoils the reconstruction (see blue lines). This gradient is due to the extremely asymmetric position of the ROI inside the sample (Kyrieleis *et al* 2011). Figure 3(c) presents the result of the iterative ROI reconstruction side by side with the phantom. Gray values are found correctly without having access to the full sinogram. Feature sharpness is clearly enhanced and comparable to the original. Furthermore, the peripheral glow appearing in (b) is visibly reduced. Finally, profiles through different iterates, i.e. through intermediate reconstruction steps are plotted in figure 3(d). During successive iterates, relative contrast is increased and the change between successive iterates is decreased (see also inlay (2) of figure 1(c)). Note, that the observed benefit in feature sharpness may not necessarily be a benefit in resolution. Further, we cannot explicitly exclude, that the loss in feature sharpness in case of the pure FBP-ansatz is a consequence of the specific implementation of FBP used in this work.

Next, the influence of the sample shape on the result of the iterative reconstruction is examined. Figure 4(a) puts the simulation of a ROI embedded in a perfectly circular sample side by side with simulations using phantoms of the same sample but with shapes deviating from a circle to different degrees (figures 4(b)–(c)). While the single step ROI reconstruction based on sinogram extension does not show significant dependence on the geometry of the sample and displays similar artifacts of peripheral glow and elevated gray values for all three cases, the iterative algorithm is capable to capture the correct gray values inside the center of the ROI in every examined configuration but shows increasing artifacts of peripheral glow toward the outer regions of the ROI with increasing deviation from the circular shape of the entire sample. This is illustrated by line profiles through phantom, single step reconstruction and iterative reconstruction displayed to the left of figures 4(a)–(c). Note that here, for clarity, the mean gray value of the single step reconstruction was shifted to that of the phantom in order to enable direct comparison of the profiles. These findings allow the conclusion that the effect of geometry correction is mainly two-fold: First, the projected gray values are reduced to the contribution of the ROI. This leads to correct mean gray values inside the reconstructed ROI. Second, geometry dependent artifacts such as peripheral glow are reduced. Once the cross-section of the full sample deviates from a circle, compensation of geometry dependent artifacts is not that efficient. Yet, the correct range of gray values inside the reconstructed ROI is less strongly affected and can be retrieved even for samples slightly deviating from a circular/cylindrical shape. In this case, however, artifacts of peripheral glow have to be corrected by different approaches. The performance of the proposed algorithm in view of even stronger deviations of the sample shape from a cylindrical geometry has not been examined within the scope of this work.

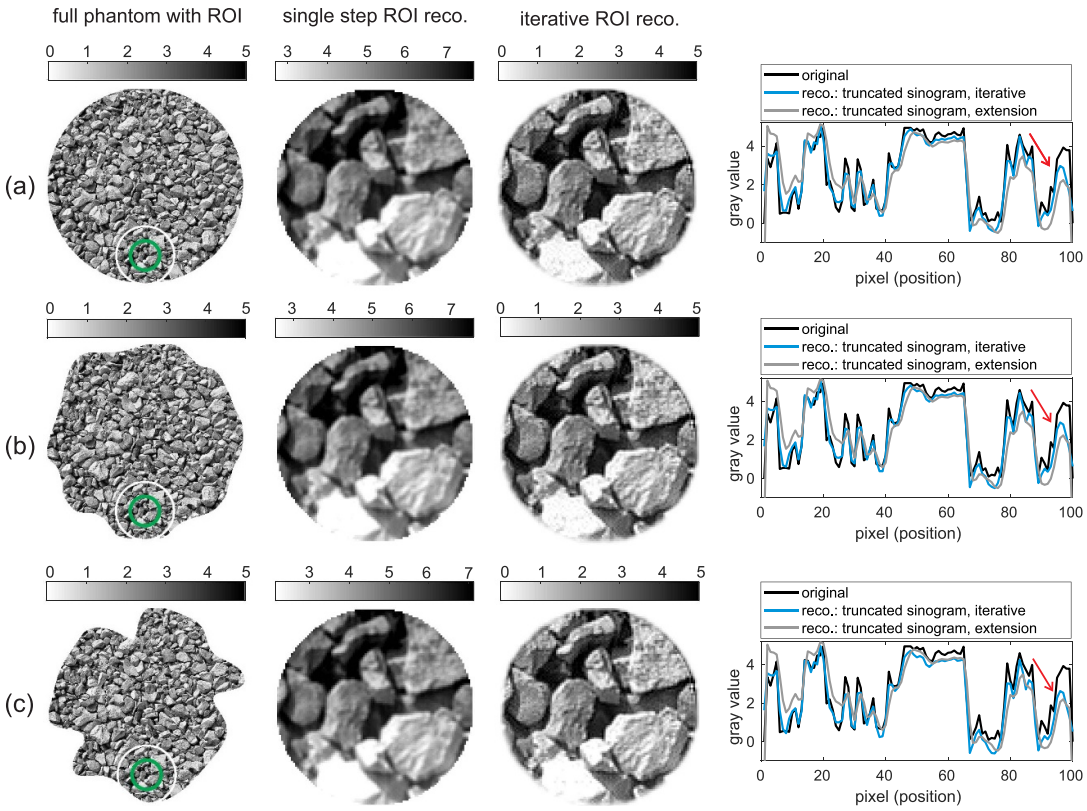

Figure 4. (a) From left to right: Phantom of circular shape with highlighted region of interest consisting of 100 pixels in diameter. Filtered back-projection of the extended truncated sinogram. Iterative reconstruction of the truncated sinogram. Color bars indicate gray values of phantom/reconstructions. Line profiles through phantom, single step (with adjusted mean gray value) and iterative reconstruction. Red arrow points to regions where increasing influence of peripheral glow can be observed. (b) Same arrangement as in (a) for a phantom slightly deviating from circular shape. (c) Same arrangement as in ((a)–(b)) for a phantom considerably deviating from circular shape.

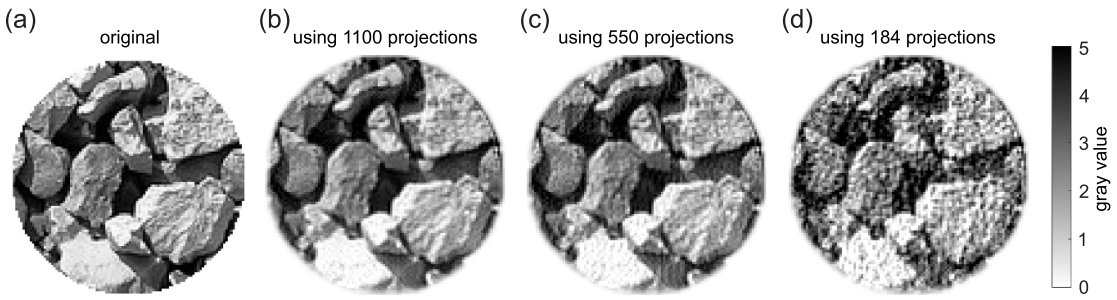

Figure 5. (a) Region of interest extracted from phantom and consisting of 100 pixels in diameter. (b) Iterative reconstruction of the truncated sinogram using 1100 projections. (c) Iterative reconstruction of the truncated sinogram using 550 projections. (d) Iterative reconstruction of the truncated sinogram using 184 projections. The displayed gray value range is the same for ((a)–(d)).

Furthermore, the influence of the number of projections on the reconstructed gray values is determined. To this end, iterative reconstruction of the truncated sinogram (figure 2((c), middle)) is performed using all 1100 projections (figure 5(b)), 550 projections (figure 5(c)) and 184 projections (figure 5(d)). Parameters for the iterative reconstruction are the same as for the simulation presented in figure 2. While for a reduced number of projections expected artifacts more and more deteriorate the reconstruction, the overall range of reconstructed gray values is not influenced compared to the original (figure 5(a)). This demonstrates that the iterative reconstruction procedure is still able to reconstruct gray values in the proper range even for a limited number of projections.

Finally, to avoid overly optimistic conclusions drawn from noise free reconstructions and to illustrate the influence of the number of iterations as well as the influence of the regions outside the ROI on the quality of

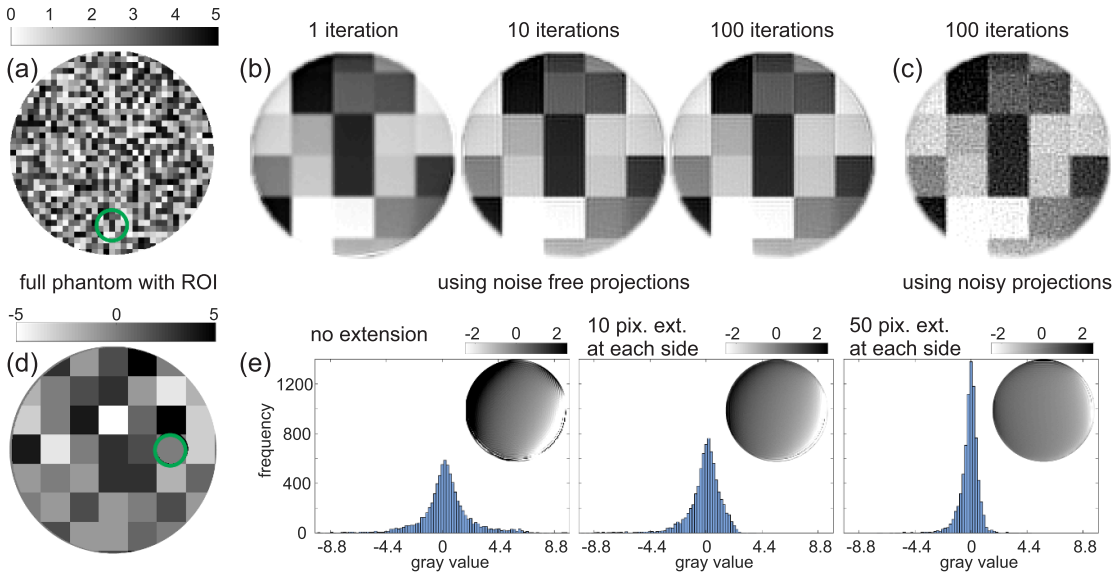

Figure 6. (a) Phantom of circular shape with highlighted region of interest consisting of 100 pixels in diameter and containing homogeneously filled quadratic regions of randomly chosen gray value. (b) Iterative reconstruction from noise free truncated sinogram terminated after one iteration, after 10 iterations and after 100 iterations. (c) Iterative reconstruction from truncated sinogram with additive Gaussian noise terminated after 100 iterations. (d) Phantom of circular shape with highlighted region of interest consisting of 100 pixels in diameter and containing homogeneously filled quadratic regions of randomly chosen gray value centered around zero gray value. The region of interest is chosen such that it contains zero gray value. (e) Influence of gray values from outside the ROI on the reconstructed ROI. Artifacts can be prevented by artificially extending the difference sinogram during iterative reconstruction. Histograms of the reconstructed gray values inside the ROI for different amount of extension. Inlays: reconstructed ROI. Color bars indicate gray values of phantom/reconstructions.

the reconstruction, a second phantom is considered: an arrangement of squares of randomly chosen gray values in the interval of $[0, 5]$ (see figure 6(a)). The remaining parameters of the simulation, the number of pixels of phantom and ROI and the number of projections are not changed. Figure 6(a) presents the phantom with highlighted and separately displayed ROI followed by (b) iterative reconstructions of noise free truncated projections stopped after 1, 10 and 100 iterations and (c) by an iterative reconstruction (100 iterations, low-pass filter kernel set to 0.47 pixels) from projections with added Gaussian noise of mean value $\mu_{\text{noise}} = 0$ and with standard deviation $\sigma_{\text{noise}} = 10$. The ratio between the standard deviation σ_{signal} of the noise free projections and σ_{noise} is $\sigma_{\text{signal}}/\sigma_{\text{noise}} \approx 25.6$. Figure 6(b) details that while edges appear blurred after the first iteration, after ten iterations, sharpness is significantly increased. Yet, inspection of the noise free reconstructions points to the necessity of avoiding overly strong transfer of high spatial frequencies in the reconstruction. This can be achieved by low-pass filtering as detailed in equation (12), or/and by terminating the reconstruction after sufficient iterations. In figure 6(c), the influence of random noise is visible. Importantly, however, neither the overall gray values of the squares, nor the general appearance of the reconstruction are impaired. Note that for this reconstruction, the low-pass filter kernel was slightly increased compared to the filter kernel used for the noise free simulations. Hence, the parameter choice of the proposed algorithm has to be balanced such that neither the positive effect of enhancement of high spatial frequencies is lost, nor noise deteriorates reconstructions.

Last but not least, the influence of regions outside the ROI on the reconstruction is examined: A phantom consisting of mean zero gray value is chosen for tomographic reconstruction from truncated projections. The ROI itself is chosen such that it is free of material and hence contains only gray values of zero. Figure 6(d) displays such a phantom. Figure 6(e) shows iterative reconstructions of the ROI. Gray values from outside the ROI particularly contaminate the edges of the reconstruction, as can be clearly seen in the left part of figure 6(e). A way out is to extend the difference sinogram during iterative reconstruction, in the same manner as the sinogram would be extended for single step reconstruction and as detailed in the description of the algorithm. The effect of extending the difference sinogram pushes artifacts outside the actual ROI and allows to achieve less contaminated reconstructions (see figure 5(e), middle and right part). The histograms in figure 5(e) demonstrate that indeed, it is possible to reconstruct gray values centered around zero nearly everywhere inside the ROI with the proposed iterative method given the fact that the mean gray value inside the sample is centered around zero and provided that the difference sinogram was extended during reconstruction.

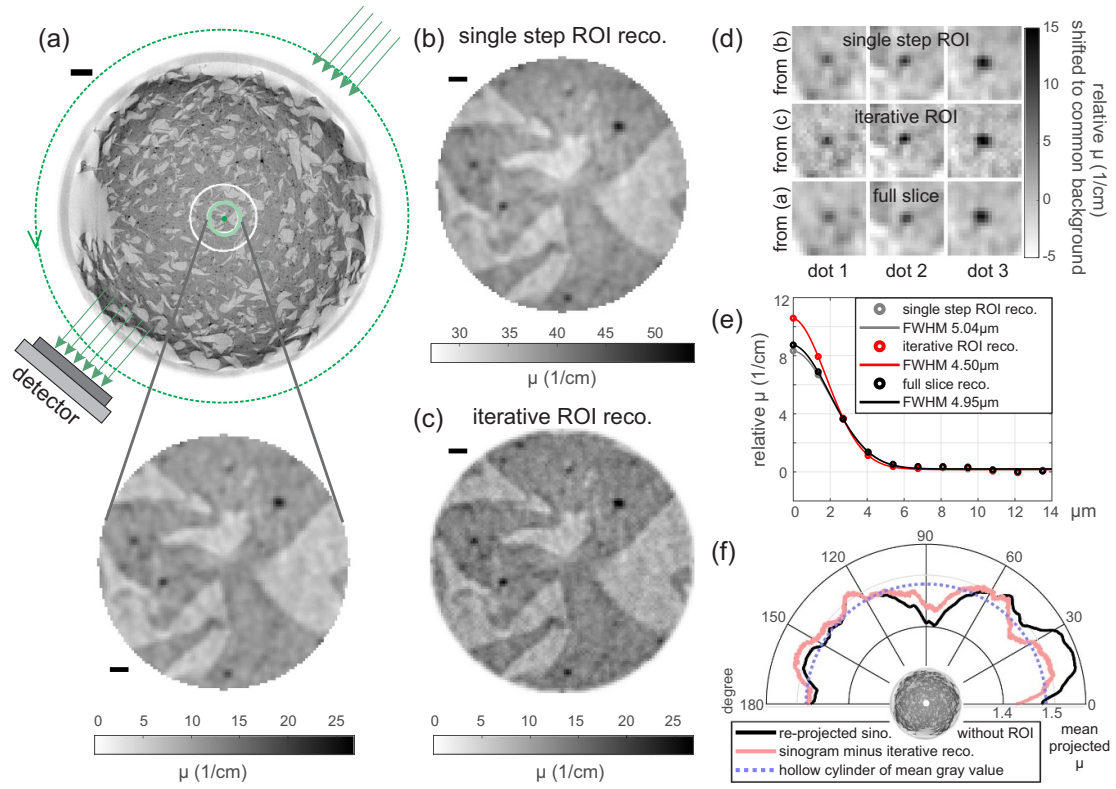

Figure 7. (a) Top: Filtered back-projection of a full sinogram from a foam sample inside a polymer tube; scale bar: 100 μm. Bottom: Zoom into the central ROI; scale bar: 10 μm. Green dot: Position of the axis of rotation. Light green circle: rFOV of ROI. (b) Reconstruction from a truncated sinogram with artificial extension; white ring in (a) marks the amount of extension; scale bar: 10 μm. (c) Iterative reconstruction from the truncated sinogram; scale bar: 10 μm. (d) Offset corrected dot structures in (top) the reconstruction based on the truncated, extended sinogram, (middle) the iterative reconstruction based on the truncated sinogram and (bottom) the reconstruction using the full sinogram. (e) Sharpness of mean dot structure (see (d)). (f) Reconstructed mean gray values outside the ROI. Dashed line: homogeneously filled hollow cylinder of background value b; black line: truncated, re-projected sinogram from sample (a) with empty ROI (see inset); light red line: truncated measured sinogram with subtracted sinogram from iterative ROI-reconstruction.

3. Local tomography of foam from an earplug

For experimental validation, the proposed method is tested on measured data. For this purpose, dense foam from an earplug is selected as a test pattern which is rich in interior structure. It is placed in a polymer tube of $d = 1.4$ mm diameter and aligned in a home-built micro-CT setup with a micro-rotating copper anode (Rigaku mm007). Acceleration voltage is set to 40 kV and the tube current to 30 mA. The sample is positioned 500 mm behind the focal spot of the rotating anode (spot size $\simeq$70 μm). Projection images are recorded with a high resolution x-ray camera (scintillator plus lens unit: XSight Micron camera model LC 0540, Rigaku) and pixel size 0.54 μm, placed 5 mm behind the sample. This minimizes blur by the source spot and justifies the assumption of parallel beam illumination. The sample is rotated from 0 deg to 180 deg (1801 projections with angular steps of 0.1 deg). Each frame contains the full sample and is exposed for 40 s. In this way, we have access the complete projections, and can compute truncated projections artificially for reconstruction. In the first step before any reconstruction, the single projections are binned to a pixel size Δ_p of 1.35 μm. Due to the tomographic sampling criterion, $d\pi/(2\Delta_p) \approx 1629$ projections are required to properly reconstruct the ROI. Hence, the tomogram is angular-wise slightly over-sampled. Reconstruction artifacts from insufficient angular sampling can thus be excluded. Single frames are pre-processed by Bronnikov-aided correction (Witte *et al* 2009) to eliminate effects of edge enhancement, see also Bartels *et al* (2013), Töpperwien *et al* (2016) for implementation of this correction at in-house micro-CT sources. The negative natural logarithm of the processed projections is used for absorption based tomography, i.e. to reconstruct the 3D distribution of the absorption coefficient μ of the sample.

Projections are low-pass filtered. The full sinogram consisting of 1319 pixels in spatial direction (after binning) is processed by a tomographic wavelet based filter for ring removal (Münch *et al* 2009).

First, a slice of the complete sample is reconstructed by FBP (see figure 7(a)). Second, the sinogram is truncated to 99 pixels symmetrically around the axis of rotation. The truncated sinogram is reconstructed twice: (i) by artificial extension of the sinogram (symmetrical addition of 118 pixels in total in the spatial

direction replicating the outermost gray values) and (ii) by iterative ROI-tomography (100 iterations, extension of the difference sinogram by approximately the same amount of pixels as used for extending the truncated sinograms for reconstruction (i)). The iterative procedure is stopped after 100 iterations, since successive iterations do not show visible differences anymore. Results are depicted in figures 7(a)–(c).

Compared to the ROI shown in (a), the iterative procedure yields correct gray values from truncated projections, i.e. in agreement with those reconstructed from the complete projections, while the single step sinogram extension technique results in systematically elevated gray values. The gain in feature sharpness observed in simulations is illustrated by three examples of dot-like structures extracted from (a–c) and shown in (d). The visible impression that iterative ROI tomography increases feature sharpness is further emphasized by comparing the full widths at half maximum of the mean angular averaged dot profiles (see (e)). Finally (f) depicts the mean projected gray values for the region outside the ROI, obtained by the differences between truncated sinograms and sinograms computed from the ROI-reconstructions. Both curves agree well despite some deviation for the projections taken under about 20 degrees.

4. Conclusion

In this work, an iterative algorithm for local tomography was introduced that is capable of reconstructing quantitative gray values. Importantly, no full projections are required. The main underlying idea is to exploit the linearity of the Radon transform and knowledge about the shape of the full sample, while minimizing the mismatch between a uniform ROI filled with constant zero gray value and the FBP from the difference between measured sinogram and forward projected current guess of gray values and structures inside the ROI. The algorithm was designed for samples of cylindrical shape and with small deviations in the index of refraction. It covers applications/samples commonly examined in the field of micro/nano-CT of biological tissues. Yet, the algorithm can be adapted to shapes of different geometry, by modeling the geometry dependent offset correction appropriately. As a positive side-effect, the algorithm does not only allow reconstructing correct gray values and reduces peripheral glow but may increase feature sharpness of the reconstruction compared to a single-step FBP approach. The extension of this algorithm to cone beam tomography is straightforward despite the design of the geometric offset correction which would require some more work. Importantly, the method is not limited to using a FBP approach: it can be combined with any tomographic reconstruction operator and its inverse. Finally, we stress that this correction scheme could be combined with overview scans recorded at different magnification, as well as with clever stitching of ROIs to extend the reconstruction, as required for challenging applications such as 3D histology of large brain regions. For example, covering a cubic millimeter of brain tissue with 50 nm resolution would be a major benchmark for neuroscience, and a correspondingly large challenge not only for data acquisition but also for ROI tomographic reconstruction.

Acknowledgment

This work was funded by Bundesministerium für Bildung und Forschung (BMBF) [Federal Ministry of Education and Research (Germany)] (project 05K19MG2).

References

Azencott R, Bodmann B G, Chowdhury T, Labate D, Sen A and Vera D 2018 ROI reconstruction from truncated cone-beam projections *Inverse Probl. Imaging* **12** 29–57

Bartels M, Hernandez V H, Krenkel M, Moser T and Salditt T 2013 Phase contrast tomography of the mouse cochlea at microfocus x-ray sources *Appl. Phys. Lett.* **103** 083703

Clackdoyle R and Defrise M 2010 Tomographic reconstruction in the 21st century *IEEE Signal Process. Mag.* **27** 60–80

da Silva J C, Guizar-Sicairos M, Holler M, Diaz A, van Bokhoven J A, Bunk O and Menzel A 2018 Quantitative region-of-interest tomography using variable field of view *Opt. Express* **26** 16752–68

Hsieh J, Chao E, Thibault J, Grekowicz B, Horst A, McOlash S and Myers T J 2004 A novel reconstruction algorithm to extend the ct scan field-of-view *Med. Phys.* **31** 2385–91

Kak A C and Slaney M 2001 *Principles of Computerized Tomographic Imaging* (Philadelphia, PA: SIAM) (https://doi.org/10.1137/1.9780898719277)

Kim J H, Kwak K Y, Park S B and Cho Z H 1985 Projection space iteration reconstruction-reprojection *IEEE Trans. Med. Imaging* **4** 139–43

Kudo H, Courdurier M, Noo F and Defrise M 2008 Tiny *a priori* knowledge solves the interior problem in computed tomography *Phys. Med. Biol.* **53** 2207–31

Kyrieleis A, Titarenko V, Ibison M, Connolley T and Withers P J 2011 Region-of-interest tomography using filtered backprojection: assessing the practical limits *J. Microsc.* **241** 69–82

Müller M and Arce G R 1996 Truncation artifacts in tomographic reconstructions from projections *Appl. Opt.* **35** 3902–14

Münch B, Trtik P, Marone F and Stampanoni M 2009 Stripe and ring artifact removal with combined wavelet—Fourier filtering *Opt. Express* **17** 8567–91
Nalcioglu O, Cho Z H and Lou R Y 1979 Limited field of view reconstruction in computerized tomography *IEEE Trans. Nucl. Sci.* **26** 546–51
Nassi M, Brody W R, Medoff B P and Macovski A 1982 Iterative reconstruction-reprojection: An algorithm for limited data cardiac-computed tomography *IEEE. Trans. Biomed. Eng.* **BME-29** 333–41
Natterer F 2001 *The Mathematics of Computerized Tomography* (Philadelphia, PA: SIAM) (https://doi.org/10.1137/1.9780898719284)
Ogawa K, Nakajima M and Yuta S 1984 A reconstruction algorithm from truncated projections *IEEE Trans. Med. Imaging* **3** 34–40
Ohnesorge B, Flohr T, Schwarz K, Heiken J P and Bae K T 2000 Efficient correction for CT image artifacts caused by objects extending outside the scan field of view *Med. Phys.* **27** 39–46
Paleo P, Desvignes M and Mirone A 2017 A practical local tomography reconstruction algorithm based on a known sub-region *J. Synchrotron Radiat.* **24** 257–68
Paleo P and Mirone A 2017 Efficient implementation of a local tomography reconstruction algorithm *Adv. Struct. Chem. Imag.* **3** 5
Radon J 1917 Über die Bestimmung von Funktionen durch ihre Integralwerte längs gewisser Mannigfaltigkeiten *Akad. Wiss.* **69** 262–77
Robisch A-L, Eckermann M, Töpperwien M, van der Meer F, Stadelmann-Nessler C and Salditt T 2020 Nanoscale x-ray holotomography of human brain tissue with phase retrieval based on multienergy recordings *J. Med. Imaging* **7** 1–13
Töpperwien M, Krenkel M, Quade F and Salditt T 2016 Laboratory-based x-ray phase-contrast tomography enables 3D virtual histology *Proc. SPIE* **9964** 996401
Töpperwien M, van der Meer F, Stadelmann C and Salditt T 2018 Three-dimensional virtual histology of human cerebellum by x-ray phase-contrast tomography *Proc. Natl. Acad. Sci. USA* **115** 6940–5
Wagner W 1979 Reconstructions from restricted region scan data—new means to reduce the patient dose *IEEE Trans. Nucl. Sci.* **26** 2866–9
Wang G and Yu H 2013 Meaning of interior tomography *Phys. Med. Biol.* **58** R161–R186
Witte Y D, Boone M, Vlassenbroeck J, Dierick M and Hoorebeke L V 2009 Bronnikov-aided correction for x-ray computed tomography *J. Opt. Soc. Am.* A **26** 890–4
Ye Y, Yu H, Wei Y and Wang G 2007 A general local reconstruction approach based on a truncated Hilbert transform *Int. J. Biomed. Imaging* **2007** 063634
Yu H, Ye Y, Zhao S and Wang G 2006 Local ROI reconstruction via generalized FBP and BPF algorithms along more flexible curves *Int. J. Biomed. Imaging* **2006** 014989
Zhang B and Zeng G L 2007 Two-dimensional iterative region-of-interest (ROI) reconstruction from truncated projection data *Med. Phys.* **34** 935–44
Ziegler A, Nielsen T and Grass M 2008 Iterative reconstruction of a region of interest for transmission tomography *Med. Phys.* **35** 1317–27